Ultrasound-assisted synthesis of ZnO photocatalysts for gas phase pollutant remediation: role of the synthetic parameters and of promotion with WO_3

Daniela Meroni[a,b,*], Cinzia Gasparini[a], Alessandro Di Michele[c], Silvia Ardizzone[a,b], Claudia L. Bianchi[a,b]

[a] *Department of Chemistry, Università degli Studi di Milano, Italy*

[b] *Consorzio INSTM, Florence, Italy*

[c] *Department of Physics and Geology, Università degli Studi di Perugia, Italy*

** Corresponding author: daniela.meroni@unimi.it*

Abstract

The synthesis of ZnO photocatalysts by ultrasound-assisted technique was here investigated. Several experimental parameters including the zinc precursor (acetate, chloride, nitrate), sonication conditions (amplitude, pulse) and post-synthetic thermal treatment (up to 500 °C) were studied. Crystalline ZnO sample were obtained without thermal treatments due to the adopted reactant ratios and synthesis temperature. Sonication plays a major role on the morphological oxide features in terms of particle size and surface area, the latter showing a 20-fold increase with respect to conventional synthesis. Interestingly, 1 and 3 s sonication pulses led to morphological properties similar to continuous sonication. A thermal treatment at moderate temperatures (400-450 °C) promoted the loss of surface hydroxylation and the formation of lattice defects, while higher temperatures were detrimental for the sample morphology. The prepared ZnO was decorated with WO_3 particles comparing an ultrasound-assisted technique using 1 s pulses with a conventional approach, giving rise to composites with promoted visible light absorption. Samples were tested towards the photocatalytic degradation of nitrogen oxides (500-1000 ppb) in humidified air under both UV and visible light. By carefully controlling the synthetic procedure, better performance were observed with respect to the commercial benchmark. Samples from ultrasound-assisted syntheses, also in the case of pulsed sonication, showed consistently better results than conventional references, in particular for ZnO-WO_3 composites. Composite by ultrasound-assisted synthesis showed > 95% degradation in 180 min and doubled NO_x degradation under visible light with respect to the conventional composite.

Keywords

Zinc oxide; ZnO-WO_3 composites; ultrasound-assisted synthesis; photocatalysis; nitrogen oxides; photo-deNOx

1. Introduction

ZnO is an environmentally friendly n-type semiconductor with a broad band gap (about 3.3. eV) and a large exciton binding energy (about 60 meV) at room temperature [1]. It is chemically and thermally stable, biocompatible and antimicrobial. Its unique physicochemical properties promote numerous and sustainable applications ranging from solar cells to sensors, from optoelectronics to biomedical devices [2–4]. The photocatalytic applications of the oxide span from hydrogen evolution to pollutants degradation in water [5–7], while the application of ZnO to the photodegradation of gaseous pollutants is instead scantly reported [8].

Nitrogen(II) oxide and nitrogen(IV) oxide, generically called NO_x, are among the major air contaminants being highly toxic for humans and vegetation, and causing environmental problems such as acid rain, photochemical smog, ozone layer depletion and greenhouse effect [9,10]. They are mainly produced by combustion processes, hence they are ubiquitous pollutants produced by a variety of anthropogenic and natural sources, and NO_x atmospheric concentrations still widely exceed quality standards in several countries [11]. While numerous studies investigate the NO_x degradation by TiO_2 [10], the degradation of NO_x by ZnO photocatalysis has been scarcely reported and it refers to either composites with other semiconductors [12–14], mixed oxides [15] or systems obtained upon complex reactions [16]. Air pollutant degradation is largely influenced by the photocatalyst morphological features, often a critical aspect of ZnO wet syntheses, especially performed without capping agents [17,18]. Hence, the development of a simple synthetic procedure enabling the facile control of ZnO features may be therefore a relevant goal for NO_x degradation.

The outstanding effects produced by sonication during synthesis on the bulk and morphological features of materials are amply reported in the literature [19]. Acoustic cavitation promotes instantaneously conditions of high temperature and pressure resulting in matchless properties of the final material [20]. Moreover, sonication can favor the formation of smaller aggregates and more homogenous coatings [21]. Literature reports about the sonochemical or ultrasound-assisted syntheses of ZnO underline the role played by sonication on the oxide morphology: Flower-like structures [22,23], nanoleaves [24], nanorods [25] and spindle-like rods [26] have been reported. In the work by Jung *et al.* [27], a sonochemical route was applied to obtain shape-selective ZnO nanostructures including nanorods, nanocups, nanodisks, nanoflowers and nanospheres. ZnO materials obtained by ultrasound-assisted reactions have been tested for different applications: water vapor permeability [22], antibacterial action [24], phenol mineralization [23] and degradation of methyl orange [19]. To the authors' best knowledge, no results relative to the application of ZnO

prepared by ultrasound-assisted procedures to the photocatalytic degradation of NO_x could be found in the literature.

As other large band gap semiconductors (> 3.0 eV), ZnO photocatalysts suffer from low efficiency under solar irradiation and even lower under visible light irradiation, as UV irradiation is required to promote the generation of charge carriers. This aspect is especially critical for indoor air remediation, as LED lamps have no UV component. Several approaches have been proposed to promote the ZnO activity under visible light, such as the formation of composites with other semiconductors [28]. Among the possible candidates, WO_3 is one of the most promising due to its chemical and photochemical stability, and its relatively narrow band gap (2.6–2.8 eV), which enables the use of longer excitation wavelengths [29]. Moreover, WO_3 band structure is suitable to form efficient heterojunctions with ZnO [30], a desired feature to promote the carrier lifetime and photocatalytic efficiency also under UV irradiation. ZnO-WO_3 composites have recently shown promising results in numerous fields, including sensing [31,32], energy storage [33], photochemical water splitting [30,34] and photocatalytic and sonocatalytic applications, mainly for wastewater treatment [12,35–38]. Gasparotto *et al.*[12] recently reported improved photocatalytic activity of ZnO-WO_3 composite films, prepared by a two step, vapor-phase route, for NO_x abatement under simulated sunlight.

Sonication has been reported to promote the preparation of efficient composites in the case of other systems [39,40]. In the case of ZnO, the sonochemical assisted formation of composites has been reported using ZnO prepared by traditional procedures [41–43]. No previous reports can be found concerning ultrasound-assisted synthesis of ZnO-WO_3 systems.

In this work, a facile synthesis of ZnO nanoparticles by ultrasound-assisted method, under ambient conditions, is reported. The role played by the nature of the metal precursor, of post-synthesis thermal treatments and of the ultrasound power density and mode (continuous/pulsed) were here investigated. In particular, the use of pulsed sonication with pulse duration as short as 1 s was investigated as an energy-saving approach. The prepared materials were extensively characterized with respect to their structural, morphological, optical and surface features. WO_3-decorated ZnO systems were also prepared by both conventional and ultrasound assisted procedures. All samples were tested towards the photocatalytic degradation of NO_x under both UV and visible light irradiation, also with respect of commercial benchmark photocatalysts.

2. Materials and methods

All of the adopted reagents were of analytical grade and were purchased from Sigma-Aldrich, unless differently specified, and used without further purification. MilliQ water was used during all experiments to prepare solutions and suspensions.

2.1 Synthesis of ZnO samples

ZnO samples were synthesized according to the following general procedure. First, 100 mL of a 0.2 M aqueous solution of a zinc precursor salt (either zinc nitrate hexahydrate, zinc chloride or zinc acetate dihydrate) was mixed with 100 mL of 0.5 M KOH aqueous solution in a 250 mL beaker and sonicated using an ultrasonic processor (Thermo-Fischer Q700), working at a fixed frequency of 20 kHz, equipped with a 13-mm diameter titanium halloy (Ti-6Al-4 V) horn immersed for *ca.* 20 mm. Sonication was conducted for an overall duration of 30 min (including on and off time for pulsed sonication), in order to maintain for each synthesis the same ageing time, which is known to affect crystal growth and particle agglomeration. The synthesis was performed in adiabatic conditions, leading to a final temperature of 70 ± 3 °C in continuous sonication tests. Different tests were carried out varying several parameters, including the power density, sonication mode (either continuous or pulsed) and pulse rate. During syntheses using pulsed sonication, each pulse was separated by a time interval of duration equal to the pulse length (*e.g.*, 1 s pulse separated by 1 s intervals). The resulting precipitate was then separated via centrifugation and washed by several centrifugation-resuspension cycles in water until neutral pH was reached, then it was dried in oven at 70 ºC. The effect of a final calcination treatment in pure O_2 flow (9 NL/h) was investigated on selected samples, adopting a heating rate of 2°C min^{-1}, 1 h at stationary temperature and calcination temperatures in the range 400-500°C.

Samples are labeled as Z*xyz_T* where *x* indicates the type of zinc precursor (NO standing for zinc nitrate hexahydrate, Cl for zinc chloride, and Ac for zinc acetate), *y* is the ultrasound power density (in W cm^{-2}), *z* indicates the sonication mode (c for continuous, p followed by a number stands for pulse and the number is the pulse duration in s), and *T* is the calcination temperature (in °C), if the latter is not indicated, the sample was submitted to no calcination post-treatment.

For the sake of comparison, a reference sample (labeled as ZNOstir) was prepared according to the same procedure using a mechanical stirring (250 rpm) instead of sonication, and keeping the reaction temperature at 65°C. Moreover, a commercial ZnO sample (Sigma-Aldrich, named Zcom in the following) was adopted as benchmark throughout the study. For the sake of clarity, Table 1 lists the adopted samples.

2.2 Synthesis of ZnO-WO_3 composites

ZnO-WO_3 composites were prepared using selected synthesized ZnO samples and WO_3 seeds prepared according to the following procedure. WO_3 seeds were synthesized using an acid precipitation technique followed by a low-temperature hydrothermal treatment. First, 40 mL of a 37% HCl solution was added drop-wise to a 1.3 mM aqueous solution of ammonium metatungstate hydrate, until formation of a yellow precipitate. Then, this solution was hydrothermally treated at 95 °C for 6 h. The obtained precipitate was collected by centrifugation and washed several times with water, then dried in oven at 70 °C overnight.

Composite samples were prepared with a 8%w WO_3 content. Two synthetic procedures were compared: in the first one, uncalcined ZnO and WO_3 seeds were dispersed in 200 mL of water and then sonicated (20 kHz, power density 38 W cm^{-2}, pulsed mode, 1 s pulse duration, overall duration 30 min) using the same experimental setup described for ZnO ultrasound-assisted synthesis. The powder was recovered by centrifugation, dried in oven at 70 °C, and calcination at 450 °C in pure O_2 flux (9 NL h^{-1}) with a heating rate of 2°C min^{-1} and 1 h at stationary temperature. For the sake of comparison, ZnO-WO_3 composite was prepared adopting a classical mechanical procedure: uncalcined ZnO and WO_3 seeds were ground together in a mortar; the powder was then calcined with the same procedure. Composites will be labeled with the name of the used ZnO sample followed by Ws and Wm for the ultrasound-assisted and mechanical routes, respectively.

2.3 Materials characterization

X-ray powder diffraction (XRD) patterns were collected using a X'Pert PRO (PANanalytical) diffractometer, operating at 40 kV × 40 mA nominal X-ray power and employing graphite-monochromated Cu Kα radiation. Diffractograms were recorded in the 20-95° 2θ range, using a step size 0.05° and scan speed 0.09 °/s. The crystallites size was estimated applying the Scherrer equation.

The specific surface area of the samples was determined by applying the Brunauer-Emmett-Teller (BET) method to the N_2 adsorption-desorption isotherms recorded at subcritical conditions using a Coulter SA3100 instrument. Pore volume and pore size distribution was determined from desorption isotherms using the Barrett, Joyner, and Halenda (BJH) method.

Scanning electron microscopy (SEM) analyses were performed using a field emission SEM microscope LEO 1525 (Zeiss) upon metallization with Cr. Images were acquired by Inlens detector while elemental composition was determined by energy dispersive X-ray analysis (EDX, Bruker Quantax).

Fourier transform infrared (FTIR) spectra were acquired on a Spectrum100 (Perkin Elmer) spectrophotometer, working in Attenuated Total Reflectance (ATR) mode. Spectra were recorded in the 4000-400 cm^{-1} range with a resolution of 4.0 cm^{-1}, averaging 12 scans.

The average particle size in water was investigated via dynamic light scattering (DLS) determinations carried out on a Zetasizer Nano ZS (Malvern Instruments) equipped with a solid state He-Ne laser (λ = 633 nm). Each hydrodynamic diameter was averaged from at least three measurements.

The sample optical properties were investigated via diffuse reflectance spectroscopy (DRS). Spectra were acquired on a UV-2600 (Shimadzu) UV-vis spectrophotometer, equipped with an integrating sphere, in the 250-800 nm range.

2.4 Photocatalytic tests

The photocatalytic activity of the prepared samples was tested towards the degradation of NO_x in gas phase, under UV and visible light irradiation using a setup operating in static condition [44,45]. Photocatalytic degradations were performed in a Pyrex glass cylindrical reactor with a 20 L effective volume. Photocatalyst films were deposited by drop-casting a suspension of in 0.050 ± 0.001 mg of oxide in i-propanol (technical grade, Sigma Aldrich) on a glass plate (200 mm x 20 mm). The gaseous mixture in the reactor was obtained by mixing NO_2 with air humidified at 40-50%. The starting inlet gas contains only NO_2, but as it comes into contact with air, the chemical equilibrium between NO and NO_2 is established. As a result, photocatalytic tests were performed on a mixture of NO and NO_2 in air. Photon source during UV light tests was provided by a 500 W halogenide lamp (Jelosil, model HG 500) emitting in the UV-A (wavelength range: 320–400 nm) and yielding an effective irradiation power on the photocatalyst surface of 20 W m^{-2}. In the case of visible light tests, a LED lamp (350 mA, 9-48 V DC, 16.8 W) with emission 400-700 nm was the photon source, set at a distance to yield 1000 lx on the sample surface. The NO_x initial concentration was 1000 ppb for the test under UVA and 500 ppb under visible light irradiation. An Ecotech Serinus 40NOx directly connected to the reactor measured the concentration of both NO and NO_2. Tests were carried out at 25 °C and irradiation duration was 3 h. Photolysis tests showed a negligible pollutant degradation (< 5% after 3 h of UV irradiation). The estimated standard deviation of NO_x concentration during independent measurements on the same sample was 1%.

3. Results and discussion

3.1 Physicochemical properties of ZnO samples

XRD patterns of uncalcined samples, irrespectively of the type of zinc precursor and sonication treatment, showed the presence only of wurtzite ZnO phase (Figures 1 and S1-S2), with similar crystallite size (*ca.* 20 nm, Table 2, column 2). The presence of well defined peaks and the absence of appreciable amorphous halo support a good degree of crystallinity also in the uncalcined samples. No peaks from impurity phases could be appreciated; interestingly, no peaks related to $Zn(OH)_2$ phases could be identified. It has been reported that, during precipitation synthesis of ZnO, $Zn(OH)_2$ species convert to ZnO with a rate that depends on both the temperature and the reaction pH [46]. Pandit *et al.* [47] reported that, during ultrasound-assisted synthesis of ZnO, the conversion of $Zn(OH)_2$ to ZnO is favored by the microthermal heating generated out of sonication energy. However, in the present case, also the reference samples prepared by a conventional synthetic approach using mechanical stirring showed similar structural properties, in good agreement with literature reports working with similar zinc precursor / KOH ratios [46,48], suggesting that the crystallization step is dominated by pH and temperature conditions. In this respect, it should be noted that tests using ammonia as precipitating agent as an alternative to KOH, resulted in powders with ε-$Zn(OH)_2$ as main component (Figure S1, labeled as ZNO38c_NH_3), despite the use of a large ammonia stoichiometric excess (1 : 6). Moreover, the use of ammonia resulted in much lower yields (25%) and in powders characterized by a much lower surface area (< 5 m^2 g^{-1}).

The influence of a thermal post-treatment on the structural features was also investigated (Figure 1), showing only a slight increase of the crystallite size for calcination temperatures up to 500 °C (Table 2, column 2). The commercial benchmark sample exhibit much larger crystallite size, more than double than the synthesized samples (Table 2, column 2).

As preferential orientation of (002) planes has been associated with surface defects in ZnO, that could affect the photocatalytic activity [49,50], the relative intensity of the (002) and (100) crystal planes was here investigated. Overall, uncalcined samples exhibited higher I(002)/I(100) ratios than calcined samples, close or higher than unity. In particular, by increasing the calcination temperature, a gradual decrease in the intensity ratio could be appreciated in the ZNO38c series, which become very close to the value for bulk, isotropic ZnO [51]. It should be noted that the uncalcined sample from the conventional synthesis (ZNOstir) exhibits the highest intensity ratio, whereas increasing the sonication amplitude results in a gradual decrease of the (002) plane intensity.

The sample surface composition was also investigated by ATR-FTIR analyses. Both calcined and uncalcined samples exhibit a main band at wavenumber lower than 600 cm^{-1}, characteristic of stretching Zn-O vibrations [52]. The less intense FTIR spectra components show instead a more

marked dependence on the calcination temperature (Figure 2). In particular, components due to physisorbed water molecules can be appreciated including the broad band at 3100-3500 cm^{-1}, generally attributed to stretching vibration of OH groups mutually interacting by hydrogen bonding, and the component at 1640 cm^{-1}, which can be related to the in plane H-O-H bending mode of undissociated water [53]. Other bands are appreciable, including one at 1470 cm^{-1}, a broad component at about 1400 cm^{-1}, a shoulder at *ca.* 1000 cm^{-1}, and an intense band at 885 cm^{-1}. Ducker *et al.* [54] reported the same components for wurtzite ZnO samples exposing $Zn(OH)_2$ at the surface, which differ from those of ε-$Zn(OH)_2$ samples. In this respect, it should be noted that the same peaks are appreciable in all uncalcined samples, irrespectively of the adopted zinc precursor (Figure S3), supporting the attribution of these peaks to surface hydroxylated species and not to impurities. All of these bands markedly decrease in intensity upon calcination at 400 °C or higher (Figures 2 and S4), consistently with the loss of physisorbed water and of surface hydroxylation upon thermal treatment [46,55].

Sonication during synthesis plays a more appreciable role on the morphological features of the samples: the uncalcined sample from conventional synthesis has a surface area lower than 0.5 $m^2\ g^{-1}$, whereas continuous sonication leads to surface area more than 20 times larger (Table 2, column 3). No significant differences can be appreciated by changing the power density and, notably, also the use of pulsed sonication retains the beneficial effect on the specific surface area. In this respect, it should be noted that sonication time during oxide syntheses is known to affect the resulting particle size [24,56,57], with a more marked effect on sample morphology in the first few minutes of sonication [57]. In addition, a marked dependence on the adopted zinc precursor is observed: while the uncalcined sample from nitrate precursor has a specific surface area of *ca.* 12 $m^2\ g^{-1}$, the sample prepared using zinc acetate and zinc chloride presents almost doubled and tripled surface area values, respectively. The effect of a thermal post-treatment depends notably on the adopted calcination temperature. Calcination up to 400 °C does not affect appreciably the specific surface area value in the case of sonicated sample, which is explained by the negligible observed increase in the crystallite size and by a slight increase in the total pore volume upon thermal treatment (Figure S5). On the other hand, in the case of the sample from the conventional synthesis, an increase of the surface area is observed possibly due to freeing of the pores. A further increase in calcination temperature reduces instead the available surface area, leading to ~50% at 500 °C.

The oxide morphology was also investigated by FESEM analyses (Figure 3 and Figure S6). As for BET results, SEM images clearly show that sonication leads to a marked effect in the oxide morphological properties, mainly in terms of average size of the aggregates (Figure 3): by comparing samples obtained using the same precursor, ZNOstir shows micrometric particles with

flower-like morphology (Figure 3c,d), whereas ZNO38c presents nanometric aggregates with star-shapes morphology (Figure 3e,f). SEM results are in good agreement with DLS analyses (*vide infra*) and could explain the observed difference in specific surface area. These results are also in accordance with the literature: very recently, Sharifalhoseini *et al.* [21] reported a marked effect of sonication at 20 kHz on the morphology of ZnO coatings deposited on steel, resulting in smaller aggregates and more homogeneous coatings. These observed differences in terms of aggregate size remain even after thermal treatment. Both samples from ultrasound-assisted and conventional synthesis show comparable morphology upon calcination at 400 °C with respect to the uncalcined sample (Figure S6). Only by increasing the calcination temperature up to 500 °C, particles become smoother, showing more defined polyhedral shape (Figure S6e,f), in agreement with the observed loss of specific surface area. It should be noted that pulsed sonication leads to similar results in terms of aggregate size for pulse duration of 3 s (Figure S6g,h); on the other hand, shorter pulses (1 s) seems to lead to polydisperse particles, with much larger aggregates (Figure S6i,l). Similar morphologies are observed when changing the sonication power density (data not shown). On the contrary, the adopted zinc precursor salt greatly affects the shape and size of ZnO particles. As already mentioned, nitrates lead to particles of *ca.* 40 nm aggregated in star-shaped clusters, which suggests growth by random aggregation [58]. Chlorides instead result in smaller (*ca.* 30 nm), rounder particles (Figure 3g,h) and acetates give rise to nanoparticles of *ca.* 40 nm in size that tend to organize in plates (Figure 3i,j). These differences suggest that, although the counter-ions of the zinc precursor are not incorporated into the oxide bulk, they nonetheless have a crucial role in directing crystal formation [46]. The Zcom sample exhibits instead a nanorod morphology with hexagonal base, which is indicative of crystal growth by oriented attachment of oxide nuclei [58].

SEM results with regard to particle size in vacuum mirror closely particle size in solution as estimated via DLS analyses (Table 2, column 4). In particular, micrometric vs. nanometric particles are detected for conventional vs. ultrasound-assisted syntheses. In this respect, pulsed samples obtained with the shortest pulse duration show polydisperse particles, with a fraction of much larger aggregates. Calcination is confirmed not to affect particle size, while the zinc precursor has a notable role on the particle size. In particular, chlorides giving rise to particle < 100 nm, which raise health and environmental concerns [9]. The sample from zinc acetate shows a main fraction of nanometric particles and a minor component of micrometric size, which can be attributed, on the grounds of SEM images, to plate structures formed by aggregating particles. The use of zinc nitrate instead gives rise to particles with an average size of *ca.* 400 nm, in good agreement with the average size of star-like aggregates shown by SEM images.

The optical properties of the samples were investigated by DRS spectroscopy. All samples exhibited the classical sigmoid-shaped light absorption of ZnO, with band gap values in the range 3.1-3.3 eV (Table 2, column 5), in good agreement with the literature [17,28,59]. The DRS spectrum of ZCl38c exhibits an extended absorption in the visible region with respect to the other samples, appreciable as a grayish color, due to titanium impurities (Figure S7); the presence of chlorides gives rise to significant degradation of the sonication probe tip, despite the use of a new tip, which are not observed in the case of the other precursors. Most notably, the absorption edge shifts upon calcination of *ca.* 0.1 eV, which is appreciable by the naked eye as a transition from a white to a yellowish powder. The decrease of the apparent band gap is stable for calcination temperatures up to 500°C and could be attributed to the formation of lattice defects in the ZnO crystal bulk [59].

3.2 Physicochemical properties of ZnO-WO_3 composites

The synthesized ZnO was used for the preparation of composites with WO_3 by mixing with tungsten oxide seeds using either an ultrasound-assisted or a conventional procedure. Here we report the results relative to composites prepared starting from ZnO sample prepared via ultrasound-assisted synthesis using pulsed sonication and nitrate precursor. All samples were finally calcined at 450 °C in order to promote the crystallization of WO_3, while preserving the desired morphological features.

XRD patterns confirm the formation of segregated crystalline WO_3 for both the adopted preparation procedures (Figure 4a). Diffractograms shows wurtzite ZnO as main phase. The average crystallite size and I(002)/I(100) ratio of the ZnO phase were almost unaltered with respect to the reference sample (22.8, 20.5 and 23.7 nm and 0.83, 0.84 and 0.90 for the pure ZnO, and conventional and ultrasound-assisted composites, respectively). In ZnO-WO_3 composites, a minor content of monoclinic crystalline WO_3 (6%w and 5%w for ZNO1p_450Wm and ZNO1p_450Ws, respectively, as determined by Rietveld method). The observed crystalline WO_3 amounts are lower than EDX results, which are comparable to the nominal WO_3 content: this observation could be possibly related to the presence of highly dispersed or poorly crystalline WO_3 particles.

In this respect, FTIR spectra show, along with the characteristic features of calcined ZnO, two intense bands at 810 and 735 cm^{-1} and a shoulder at 660 cm^{-1} (Figure S8); these features are characteristic of monoclinic WO_3 and can be attributed to stretching modes of W-O-W [60,61]. No bands related to W-OH and W=O stretching modes are appreciable, supporting the absence of hydrated tungsten species and of surface wolframyl species [29,60], which have been related to poor photocatalytic performance [62].

As observed in the case of ZnO synthesis, the use of ultrasound notably affects the morphological properties. In particular, the specific surface area of the two composites is remarkably different: while the sample from the conventional synthesis shows a lower surface area with respect to the reference ZnO sample (6.9 m^2 g^{-1} *vs.* 10.8 m^2 g^{-1}), the composite from the ultrasound-assisted procedure presents a higher surface area of 13.0 m^2 g^{-1}. These data can be rationalized considering the FESEM images.

SEM images of the reference sample (Figure S9a,b) show the star-shaped aggregates, of *ca.* 300 nm in size, characteristic of nitrate precursor; the effect of the calcination step is clearly appreciable as individual particles appear rather smooth and prismatic in shape. The composite from the conventional synthesis presents a rather similar morphology (Figure S9c,d), whereas in the composite from ultrasound-assisted procedure (Figure S9e,f), the star-shaped aggregates are not clearly appreciable, as they appear covered by smaller individual nanoparticles bestowing a rougher surface texture.

DRS spectra (Figure 4b) clearly show an enhanced visible light absorption for ZnO-WO_3 composites with respect to the ZnO reference sample. In particular, a visible light absorption in the 400-500 nm region can be appreciated, which is responsible for the yellow color of the composites. First-derivative graphs (Figure S10) clearly show a main peak at 3.20 eV for all samples that corresponds to the band gap of the main ZnO phase, which does not shift upon WO_3 addition; this observation supports the absence of diffusion of W species within the ZnO lattice [63], which could impair the photocatalytic activity by promoting recombination. In the ZnO-WO_3 composites, a second component centered at 2.76 eV can be appreciated, in good agreement with the band gap of WO_3 [29,30].

3.3 Photocatalytic activity

The photocatalytic activity of all samples was tested towards the degradation of NO_x in air. Tests under UV irradiation for the pristine ZnO samples showed a marked effect of ultrasound on the photocatalytic activity (Figure 5a): samples from conventional synthesis present a much slower degradation kinetics than the relative oxides prepared via ultrasound-assisted technique. Even after 180 min of irradiation, only 58% of NO_x has been degraded during tests with ZNOstir with respect to 79% using ZNO38c. This difference is still appreciable even in calcined samples and could be related to the different morphological features of samples from conventional and ultrasound-assisted syntheses. In particular, the larger surface area of the latter promotes the photocatalytic activity, in good agreement with literature reports about gas phase photocatalytic reactions[64][10].

Modifying the ultrasound power density has a slight effect on the photocatalytic activity, particularly if the amplitude is increased (Figure S11), in accordance with the similar physicochemical characteristics exhibited by these samples (see Section 3.2).

However, tests on samples prepared using different precursors prove that the surface area is not the only factor at play: ZCl38c, which has the largest surface area among the tested samples, shows a faster NO_x degradation than ZNO38c, whereas ZAc38c, despite its quite large surface area (18 m^2 g^{-1}) displays a mere 72% of NO_x degradation after 3 h.

Most interestingly, a post-synthetic thermal treatment has a notable effect on the photocatalytic degradation (Figure 5c). Moderate calcination temperatures (up to 450 °C) markedly promote the photocatalytic activity (> 90% NO_x degradation after 180 min of irradiation). It should be noted that the sample calcined at 450 °C exhibits an enhanced photocatalytic activity with respect to the uncalcined sample, despite its lower surface area. Therefore, the promoting effect of the calcination step can be related to the change in structural properties: while no notable changes in the phase composition and crystallite size can be observed among samples uncalcined and calcined at $T \geq 450$ °C, the I(002)/I(100) ratio, FTIR spectra and absorption edge exhibit notable differences. The observed changes can possibly be related to surface rearrangements exposing more active facets [51], despite the formation of lattice defects that can act as recombination centers [65]. The loss of surface hydroxylation can also impact the NO_x surface adsorption. It is noteworthy that the calcined samples outperform the commercial benchmark sample, especially at short irradiation time. A further increase in the calcination temperature causes a further decrease in surface area that outweighs the structural benefits, leading to a detrimental effect on the photocatalytic properties (Figure 5c).

In order to reduce the energy cost of the preparation technique, pulsed sonication was compared to continuous sonication. Pulsed sonication with pulse duration as low as 3 s leads to minor effects in terms of photocatalytic activity, which remains almost unchanged with respect to the sample from continuous sonication, particularly at short irradiation time (Figure S12). A further decrease in pulse duration causes a slight decrease in photocatalytic activity, which could be related to the higher aggregation degree observed by SEM and DLS.

The preparation of ZnO-WO_3 composites further promotes the photocatalytic activity under UV irradiation, achieving *ca.* 95% degradation after 180 min of irradiation (Figure 6a). Also in this case, the use of ultrasound during synthesis, in particular during the mixing of the two semiconductors, promotes the photocatalytic activity, giving rise to 73% NO_x degradation after 60 min with respect to 64% for the conventional composite.

The $ZnO-WO_3$ composites were also tested using visible light irradiation, in particular using a commercial LED lamp for indoor lightning. In this case, the promoting effect of ultrasound treatment is even more marked. The visible-light photocatalytic activity of the conventional composite is comparable to the ZnO reference sample, giving rise to merely a 15% degradation after 3 h, whereas the degradation is doubled using the $ZnO-WO_3$ composite prepared by ultrasound-assisted synthesis (Figure 6b). This result can be related to the visible light absorption of the sample, coupled with its morphological features and it is possibly an indication of a better contact between the two semiconductors, as supported by SEM images.

Direct comparisons with literature data about NO_x abatement are difficult to draw as the only available reference relative to $ZnO-WO_3$ composites [12] uses largely different samples (CVD films) and experimental conditions (only simulated solar light irradiation, flow tests, shorter test duration and lower pollutant concentration). Hence, it is more sensible to compare the relative improvement of the ZnO photocatalytic activity observed upon formation of the composite with WO_3. In this respect, our study shows a much larger enhancement in the photocatalytic activity both under UV and visible light irradiation (48% and 100%, respectively) with respect to the literature (29% [12]).

4. Conclusions

In this work, we investigated an ultrasound-assisted procedure for the preparation of efficient photocatalysts for the removal of NO_x. The use of sonication enabled us to control the morphological features of the oxide, in particular with respect to the surface area and the aggregate dimension, improving the photocatalytic performance with respect to samples from conventional synthesis. Conversely, no clear effect of sonication on the oxide structural properties was observed, supporting in this respect a main role played by pH and the reaction temperature in the precipitation of $Zn(OH)_2$ and subsequent conversion to ZnO.

The counter-ion in the zinc precursor also induced relevant modifications of the morphology (star-shaped, flower-like, platelets) and surface area, even though they were not retained in the final product. Samples from chloride precursor presented very small aggregate size (< 100 nm) and appeared to promote fast dissolution of the titanium alloy probe tip; therefore, notwithstanding the fast NO_x removal, they were not adopted as reference for subsequent investigations. Acetates gave rise to less efficient photocatalytic performance. Consequently, zinc nitrate were adopted as a starting material throughout the study.

A post-synthetic thermal treatment was not required to achieve crystalline ZnO, nonetheless samples calcined at 400-450 °C showed better photocatalytic performance with respect to the

relative uncalcined sample. Despite the slight decrease in surface area consequent to calcination, improved activity was observed and possibly related to the change in surface features and microstructural properties.

Synthetic tests performed with pulsed sonication proved that pulse durations as short as 1 s provided only a slight decrease in the photocatalytic efficiency with respect to the continuous mode but, notably, at a fraction of the energy consumption.

In order to further promote the photocatalytic activity of ZnO, especially under visible light irradiation, ZnO samples were decorated with WO_3. On the grounds of energy efficiency considerations, a ZnO sample prepared by pulsed sonication was here selected as starting material for the composite preparation. The resulting composites showed visible-light absorption. Moreover, when an ultrasound-assisted procedure using pulsed sonication was adopted for the composite preparation, better morphological properties were observed with respect to both the pristine ZnO reference and the composite prepared by conventional synthesis. As a result, enhanced performance of the ultrasound-assisted composite was observed under UV irradiation. Even more promisingly, we proved for the first time the visible-light driven photocatalytic degradation of NOx by ZnO-WO_3 photocatalysts, showing at the same time a two-fold increase of NO_x degradation for composites prepared by an ultrasound-assisted procedure with respect to conventional ones. The present materials are promising photocatalysts for removal of air pollutants, even in demanding applications such as indoor remediation.

Funding

This research did not receive any specific grant from funding agencies in the public, commercial, or not-for-profit sectors.

References

[1] R.S. Yadav, P. Mishra, A.C. Pandey, Growth mechanism and optical property of ZnO nanoparticles synthesized by sonochemical method, Ultrason. Sonochem. 15 (2008) 863–868. https://doi.org/10.1016/j.ultsonch.2007.11.003.

[2] S. Aghabeygi, M. Khademi-Shamami, ZnO/ZrO2 nanocomposite: Sonosynthesis, characterization and its application for wastewater treatment, Ultrason. Sonochem. 41 (2018) 458–465. https://doi.org/10.1016/j.ultsonch.2017.09.020.

[3] X. Zhou, Y. Zou, J. Ma, X. Cheng, Y. Li, Y. Deng, D. Zhao, Cementing Mesoporous ZnO with Silica for Controllable and Switchable Gas Sensing Selectivity, Chem. Mater. 31 (2019) 8112–8120. https://doi.org/10.1021/acs.chemmater.9b02844.

[4] Z. Li, R. Wang, J. Xue, X. Xing, C. Yu, T. Huang, J. Chu, K.L. Wang, C. Dong, Z. Wei, Y. Zhao, Z.K. Wang, Y. Yang, Core-Shell ZnO@SnO2 Nanoparticles for Efficient Inorganic

Perovskite Solar Cells, J. Am. Chem. Soc. 141 (2019) 17610–17616. https://doi.org/10.1021/jacs.9b06796.

[5] X. Zhang, Y.Z. Zhou, D.Y. Wu, X.H. Liu, R. Zhang, H. Liu, C.K. Dong, J. Yang, S.A. Kulinich, X.W. Du, ZnO nanosheets with atomically thin ZnS overlayers for photocatalytic water splitting, J. Mater. Chem. A. 6 (2018) 9057–9063. https://doi.org/10.1039/c8ta01846d.

[6] H. Song, X. Meng, S. Wang, W. Zhou, X. Wang, T. Kako, J. Ye, Direct and Selective Photocatalytic Oxidation of CH4 to Oxygenates with O2 on Cocatalysts/ZnO at Room Temperature in Water, J. Am. Chem. Soc. 141 (2019) 20507–20515. https://doi.org/10.1021/jacs.9b11440.

[7] D. Neena, M. Humayun, W. Zuo, C.S. Liu, W. Gao, D.J. Fu, Hierarchical hetero-architectures of in-situ g-C3N4-coupled Fe-doped ZnO micro-flowers with enhanced visible-light photocatalytic activities, Appl. Surf. Sci. 506 (2020) 145017. https://doi.org/10.1016/j.apsusc.2019.145017.

[8] J. Liu, P. Wang, W. Qu, H. Li, L. Shi, D. Zhang, Nanodiamond-decorated ZnO catalysts with enhanced photocorrosion-resistance for photocatalytic degradation of gaseous toluene, Appl. Catal. B Environ. 257 (2019) 117880. https://doi.org/10.1016/j.apcatb.2019.117880.

[9] G. Cerrato, F. Galli, D.C. Boffito, L. Operti, C.L. Bianchi, Correlation preparation parameters/activity for microTiO2 decorated with SilverNPs for NOx photodegradation under LED light, Appl. Catal. B Environ. 253 (2019) 218–225. https://doi.org/10.1016/j.apcatb.2019.04.056.

[10] J. Lasek, Y.H. Yu, J.C.S. Wu, Removal of NOx by photocatalytic processes, J. Photochem. Photobiol. C Photochem. Rev. 14 (2013) 29–52. https://doi.org/10.1016/j.jphotochemrev.2012.08.002.

[11] EEA, Air quality 2018 - EEA report 12 2018, 2018. https://doi.org/10.2800/777411.

[12] A. Gasparotto, G. Carraro, C. Maccato, C. Sada, J. Balbuena, M. Cruz-Yusta, L. Sánchez, N. Vodišek, U. Lavrencic Štangar, D. Barreca, WO3-decorated ZnO nanostructures for light-activated applications, CrystEngComm. 20 (2018) 1282–1290. https://doi.org/10.1039/c7ce02148h.

[13] N. Todorova, T. Giannakopoulou, K. Pomoni, J. Yu, T. Vaimakis, C. Trapalis, Photocatalytic NOx oxidation over modified ZnO/TiO2 thin films, Catal. Today. 252 (2015) 41–46. https://doi.org/10.1016/j.cattod.2014.11.008.

[14] Y. Wei, Y. Huang, J. Wu, M. Wang, C. Guo, D. Qiang, S. Yin, T. Sato, Synthesis of hierarchically structured ZnO spheres by facile methods and their photocatalytic deNOx properties, J. Hazard. Mater. 248–249 (2013) 202–210. https://doi.org/10.1016/j.jhazmat.2013.01.012.

[15] M. Sarkarat, S. Komarneni, Z. Rezvani, X. Wu, S. Yin, TsugioSato, Z.F. Yan, Multi-cationic layered double hydroxides: Calcined products as photocatalysts for decomposition of NOx, Appl. Clay Sci. 80–81 (2013) 390–397. https://doi.org/10.1016/j.clay.2013.07.002.

[16] E. Kowsari, B. Bazri, Synthesis of rose-like ZnO hierarchical nanostructures in the presence of ionic liquid/Mg2+ for air purification and their shape-dependent photodegradation of SO2, NOx, and CO, Appl. Catal. A Gen. 475 (2014) 325–334. https://doi.org/10.1016/j.apcata.2014.01.046.

[17] V. Pifferi, G. Cappelletti, S. Ardizzone, L. Falciola, C. Di Bari, F. Spadavecchia, D. Meroni, A. Carrà, G. Cerrato, S. Morandi, E. Davoli, Applied Catalysis B : Environmental Photo-mineralization of noxious o -toluidine water pollutant by nano-ZnO : The role of the oxide surface texture on the kinetic path, "Applied Catal. B, Environ. 178 (2015) 233–240. https://doi.org/10.1016/j.apcatb.2014.08.043.

[18] R. Kumar, O. Al-Dossary, G. Kumar, A. Umar, Zinc oxide nanostructures for NO2 gas–sensor applications: A review, Nano-Micro Lett. 7 (2015) 97–120. https://doi.org/10.1007/s40820-014-0023-3.

[19] R. Mahdavi, S.S. Ashraf Talesh, The effect of ultrasonic irradiation on the structure, morphology and photocatalytic performance of ZnO nanoparticles by sol-gel method, Ultrason. Sonochem. 39 (2017) 504–510. https://doi.org/10.1016/j.ultsonch.2017.05.012.

[20] P. Louyot, C. Neagoe, F. Galli, C. Pirola, G.S. Patience, D.C. Boffito, Ultrasound-assisted impregnation for high temperature Fischer-Tropsch catalysts, Ultrason. Sonochem. 48 (2018) 523–531. https://doi.org/10.1016/j.ultsonch.2018.06.017.

[21] Z. Sharifalhoseini, M.H. Entezari, M. Shahidi, Sonication affects the quantity and the morphology of ZnO nanostructures synthesized on the mild steel and changes the corrosion protection of the surface, Ultrason. Sonochem. 41 (2018) 492–502. https://doi.org/10.1016/j.ultsonch.2017.10.012.

[22] Y. Bao, L. Gao, C. Feng, J. Ma, W. Zhang, C. Liu, D. Simion, Sonochemical synthesis of flower-like ZnO assembled by hollow cones toward water vapor permeability and water resistance enhancement of waterborne film, J. Ind. Eng. Chem. 82 (2019) 180–189. https://doi.org/10.1016/j.jiec.2019.10.011.

[23] O. Carp, A. Tirsoaga, R. Ene, A. Ianculescu, R.F. Negrea, P. Chesler, G. Ionita, R. Birjega, Facile, high yield ultrasound mediated protocol for ZnO hierarchical structures synthesis: Formation mechanism, optical and photocatalytic properties, Ultrason. Sonochem. 36 (2017) 326–335. https://doi.org/10.1016/j.ultsonch.2016.12.005.

[24] A. Gupta, R. Srivastava, Zinc oxide nanoleaves: A scalable disperser-assisted sonochemical approach for synthesis and an antibacterial application, Ultrason. Sonochem. 41 (2018) 47–58. https://doi.org/10.1016/j.ultsonch.2017.09.029.

[25] A. Khorsand Zak, W.H.A. Majid, H.Z. Wang, R. Yousefi, A. Moradi Golsheikh, Z.F. Ren, Sonochemical synthesis of hierarchical ZnO nanostructures, Ultrason. Sonochem. 20 (2013) 395–400. https://doi.org/10.1016/j.ultsonch.2012.07.001.

[26] Q. Liu, E. Liu, J. Li, Y. Qiu, R. Chen, Rapid ultrasonic-microwave assisted synthesis of spindle-like Ag/ZnO nanostructures and their enhanced visible-light photocatalytic and antibacterial activities, Catal. Today. 339 (2020) 391–402. https://doi.org/10.1016/j.cattod.2019.01.017.

[27] S.H. Jung, E. Oh, K.H. Lee, Y. Yang, C.G. Park, W. Park, S.H. Jeong, Sonochemical preparation of shape-selective ZnO nanostructures, Cryst. Growth Des. 8 (2008) 265–269. https://doi.org/10.1021/cg070296l.

[28] G. Cappelletti, V. Pifferi, S. Mostoni, L. Falciola, C. Di Bari, F. Spadavecchia, Hazardous o -toluidine mineralization by photocatalytic bismuth doped ZnO slurries †, Chem. Commun. 51 (2015) 10459–10462. https://doi.org/10.1039/C5CC02620B.

[29] H. Khan, M.G. Rigamonti, G.S. Patience, D.C. Boffito, Spray dried TiO2/WO3 heterostructure for photocatalytic applications with residual activity in the dark, Appl. Catal. B Environ. 226 (2018) 311–323. https://doi.org/10.1016/j.apcatb.2017.12.049.

[30] Y. Chen, L. Wang, R. Gao, Y.C. Zhang, L. Pan, C. Huang, K. Liu, X.Y. Chang, X. Zhang, J.J. Zou, Polarization-Enhanced direct Z-scheme ZnO-WO3-x nanorod arrays for efficient piezoelectric-photoelectrochemical Water splitting, Appl. Catal. B Environ. 259 (2019) 118079. https://doi.org/10.1016/j.apcatb.2019.118079.

[31] J. Han, T.Y. Wang, T.T. Li, H. Yu, Y. Yang, X.T. Dong, Enhanced NO x Gas Sensing Properties of Ordered Mesoporous WO 3 /ZnO Prepared by Electroless Plating, Adv. Mater. Interfaces. 5 (2018) 1–9. https://doi.org/10.1002/admi.201701167.

[32] Y.C. Liang, C.W. Chang, Improvement of ethanol gas-sensing responses of ZnO–WO3 composite nanorods through annealing induced local phase transformation, Nanomaterials. 9 (2019). https://doi.org/10.3390/nano9050669.

[33] Z. Bi, X. Li, Y. Chen, X. Xu, S. Zhang, Q. Zhu, Bi-functional flexible electrodes based on tungsten trioxide/zinc oxide nanocomposites for electrochromic and energy storage applications, Electrochim. Acta. 227 (2017) 61–68. https://doi.org/10.1016/j.electacta.2017.01.003.

[34] D. Barreca, G. Carraro, A. Gasparotto, C. Maccato, T. Altantzis, C. Sada, K. Kaunisto, T.P. Ruoko, S. Bals, Vapor Phase Fabrication of Nanoheterostructures Based on ZnO for Photoelectrochemical Water Splitting, Adv. Mater. Interfaces. 4 (2017) 1–9. https://doi.org/10.1002/admi.201700161.

[35] E. Mugunthan, M.B. Saidutta, P.E. Jagadeeshbabu, Photocatalytic activity of ZnO-WO3 for diclofenac degradation under visible light irradiation, J. Photochem. Photobiol. A Chem. 383 (2019) 111993. https://doi.org/10.1016/j.jphotochem.2019.111993.

[36] Y.M. Hunge, M.A. Mahadik, A. V. Moholkar, C.H. Bhosale, Photoelectrocatalytic degradation of phthalic acid using spray deposited stratified WO 3 /ZnO thin films under sunlight illumination, Appl. Surf. Sci. 420 (2017) 764–772. https://doi.org/10.1016/j.apsusc.2017.05.221.

[37] Y.M. Hunge, A.A. Yadav, V.L. Mathe, Ultrasound assisted synthesis of WO3-ZnO nanocomposites for brilliant blue dye degradation, Ultrason. Sonochem. 45 (2018) 116–122. https://doi.org/10.1016/j.ultsonch.2018.02.052.

[38] S.M. Lam, J.C. Sin, A.Z. Abdullah, A.R. Mohamed, Sunlight responsive WO3/ZnO nanorods for photocatalytic degradation and mineralization of chlorinated phenoxyacetic acid herbicides in water, J. Colloid Interface Sci. 450 (2015) 34–44. https://doi.org/10.1016/j.jcis.2015.02.075.

[39] B. Neppolian, A. Bruno, C.L. Bianchi, M. Ashokkumar, Graphene oxide based Pt-TiO2 photocatalyst: Ultrasound assisted synthesis, characterization and catalytic efficiency, Ultrason. Sonochem. 19 (2012) 9–15. https://doi.org/10.1016/j.ultsonch.2011.05.018.

[40] B. Neppolian, S. Mine, Y. Horiuchi, C.L. Bianchi, M. Matsuoka, D.D. Dionysiou, M. Anpo, Efficient photocatalytic degradation of organics present in gas and liquid phases using Pt-TiO2/Zeolite (H-ZSM), Chemosphere. 153 (2016) 237–243. https://doi.org/10.1016/j.chemosphere.2016.03.063.

[41] M. Weiße, C. Schmidt, A. Abramova, Y. Voitov, M. Stelter, P. Braeutigam, Sonochemical coating: Effect of energy input and distance on the functionalization of textiles with TiO2 and ZnO-Nanoparticles, Ultrason. Sonochem. 60 (2020) 104801. https://doi.org/10.1016/j.ultsonch.2019.104801.

[42] P. Shaikshavali, T. Madhusudana Reddy, T. Venu Gopal, G. Venkataprasad, V.S. Kotakadi, V.N. Palakollu, R. Karpoormath, A simple sonochemical assisted synthesis of nanocomposite (ZnO/MWCNTs) for electrochemical sensing of Epinephrine in human serum and pharmaceutical formulation, Colloids Surfaces A Physicochem. Eng. Asp. 584 (2020) 124038. https://doi.org/10.1016/j.colsurfa.2019.124038.

[43] N. Perkas, P. Gunawan, G. Amirian, Z. Wang, Z. Zhong, A. Gedanken, The sonochemical approach improves the CuO-ZnO/TiO2 catalyst for WGS reaction, Phys. Chem. Chem. Phys. 16 (2014) 7521–7530. https://doi.org/10.1039/c3cp55307h.

[44] C.L. Bianchi, C. Pirola, F. Galli, G. Cerrato, S. Morandi, V. Capucci, Pigmentary TiO2: A challenge for its use as photocatalyst in NOx air purification, Chem. Eng. J. 261 (2015) 76–82. https://doi.org/10.1016/j.cej.2014.03.078.

[45] C.L. Bianchi, C. Pirola, E. Selli, S. Biella, Photocatalytic NO x abatement: The role of the material supporting the TiO 2 active layer, J. Hazard. Mater. 211–212 (2012) 203–207. https://doi.org/10.1016/j.jhazmat.2011.10.095.

[46] A. Moezzi, M. Cortie, A. McDonagh, Aqueous pathways for the formation of zinc oxide nanoparticles, Dalt. Trans. 40 (2011) 4871–4878. https://doi.org/10.1039/c0dt01748e.

[47] A.B. Pandit, A.U. Badnore, Effect of pH on sonication assisted synthesis of ZnO nanostructures: Process details, Chem. Eng. Process. Process Intensif. 122 (2017) 235–244. https://doi.org/10.1016/j.cep.2017.09.013.

[48] M. Gancheva, M. Markova-Velichkova, G. Atanasova, D. Kovacheva, I. Uzunov, R. Cukeva, Design and photocatalytic activity of nanosized zinc oxides, Appl. Surf. Sci. 368 (2016) 258–266. https://doi.org/10.1016/j.apsusc.2016.01.211.

[49] E. Luévano-Hipólito, L.M. Torres-Martínez, Sonochemical synthesis of ZnO nanoparticles and its use as photocatalyst in H2 generation, Mater. Sci. Eng. B Solid-State Mater. Adv. Technol. 226 (2017) 223–233. https://doi.org/10.1016/j.mseb.2017.09.023.

[50] Y. Liu, H. Liu, Q. Zhang, T. Li, Adjusting the proportions of {0001} facets and high-index facets of ZnO hexagonal prisms and their photocatalytic activity, RSC Adv. 7 (2017) 3515–3520. https://doi.org/10.1039/c6ra24912d.

[51] A. Mclaren, T. Valdes-Solis, G. Li, S.C. Tsang, Shape and size effects of ZnO nanocrystals on photocatalytic activity, J. Am. Chem. Soc. 131 (2009) 12540–12541. https://doi.org/10.1021/ja9052703.

[52] D. Ghica, I.D. Vlaicu, M. Stefan, L.C. Nistor, S. V. Nistor, On the agent role of Mn 2+ in redirecting the synthesis of Zn(OH) 2 towards nano-ZnO with variable morphology, RSC Adv. 6 (2016) 106732–106741. https://doi.org/10.1039/c6ra23065b.

[53] G. Soliveri, V. Pi, R. Annunziata, L. Rimoldi, V. Aina, G. Cerrato, L. Falciola, G. Cappelletti, D. Meroni, Alkylsilane − SiO 2 Hybrids. A Concerted Picture of Temperature E ff ects in Vapor Phase Functionalization, J. Phys. 119 (2015) 15390–15400. https://doi.org/10.1021/acs.jpcc.5b04048.

[54] N.J. Nicholas, G. V. Franks, W.A. Ducker, The mechanism for hydrothermal growth of zinc oxide, CrystEngComm. 14 (2012) 1232–1240. https://doi.org/10.1039/c1ce06039b.

[55] D.H. Piva, R.H. Piva, M.C. Rocha, J.A. Dias, O.R.K. Montedo, I. Malavazi, M.R. Morelli, Antibacterial and photocatalytic activity of ZnO nanoparticles from Zn(OH)2 dehydrated by azeotropic distillation, freeze drying, and ethanol washing, Adv. Powder Technol. 28 (2017) 463–472. https://doi.org/10.1016/j.apt.2016.11.001.

[56] D. V. Pinjari, K. Prasad, P.R. Gogate, S.T. Mhaske, A.B. Pandit, Synthesis of titanium dioxide by ultrasound assisted sol-gel technique: Effect of calcination and sonication time, Ultrason. Sonochem. 23 (2015) 185–191. https://doi.org/10.1016/j.ultsonch.2014.10.017.

[57] V. Jafari, A. Allahverdi, M. Vafaei, Ultrasound-assisted synthesis of colloidal nanosilica from silica fume: Effect of sonication time on the properties of product, Adv. Powder Technol. 25 (2014) 1571–1577. https://doi.org/10.1016/j.apt.2014.05.011.

[58] S. Sepulveda-Guzman, B. Reeja-Jayan, E. de la Rosa, A. Torres-Castro, V. Gonzalez-Gonzalez, M. Jose-Yacaman, Synthesis of assembled ZnO structures by precipitation method in aqueous media, Mater. Chem. Phys. 115 (2009) 172–178. https://doi.org/10.1016/j.matchemphys.2008.11.030.

[59] Y. Peng, Y. Wang, Q.G. Chen, Q. Zhu, A.W. Xu, Stable yellow ZnO mesocrystals with efficient visible-light photocatalytic activity, CrystEngComm. 16 (2014) 7906–7913. https://doi.org/10.1039/c4ce00695j.

[60] C. Guéry, C. Choquet, F. Dujeancourt, J.M. Tarascon, J.C. Lassègues, Infrared and X-ray studies of hydrogen intercalation in different tungsten trioxides and tungsten trioxide hydrates, J. Solid State Electrochem. 1 (1997) 199–207. https://doi.org/10.1007/s100080050049.

[61] U. Opara Krašovec, A. Šurca Vuk, B. Orel, IR spectroscopic studies of charged-discharged crystalline WO3 films, Electrochim. Acta. 46 (2001) 1921–1929. https://doi.org/10.1016/S0013-4686(01)00361-9.

[62] L. Rimoldi, A. Giordana, G. Cerrato, E. Falletta, D. Meroni, Insights on the photocatalytic degradation processes supported by TiO 2 /WO 3 systems. The case of ethanol and tetracycline, Catal. Today. 328 (2019) 210–215. https://doi.org/10.1016/j.cattod.2018.11.035.

[63] J. Chu, X.Y. Peng, K. Dasari, R. Palai, P. Feng, The shift of optical band gap in W-doped ZnO with oxygen pressure and doping level, Mater. Res. Bull. 54 (2014) 73–77. https://doi.org/10.1016/j.materresbull.2014.03.005.

[64] O.O. Prieto-Mahaney, N. Murakami, R. Abe, B. Ohtani, Correlation between photoeatalytic activities and structural and physical properties of titanium(IV) oxide powders, Chem. Lett. 38 (2009) 238–239. https://doi.org/10.1246/cl.2009.238.

[65] D. Chen, Z. Wang, T. Ren, H. Ding, W. Yao, R. Zong, Y. Zhu, Influence of defects on the photocatalytic activity of ZnO, J. Phys. Chem. C. 118 (2014) 15300–15307. https://doi.org/10.1021/jp5033349.

Table 1. ZnO samples with their main synthetic parameters.

sample	***Zn precursor***	***power density ($W\ cm^{-2}$)***	***sonication mode***	***pulse duration (s)***	***calcination T (°C)***
Zcom	-	-	-	-	-
ZNOstir	nitrate	-	-	-	-
ZNOstir_400	nitrate	-	-	-	400
ZNO23c	nitrate	23	continuous	-	-
ZNO38c	nitrate	38	continuous	-	-
ZNO49c	nitrate	49	continuous	-	-
ZCl38c	chloride	38	continuous	-	-
ZAc38c	acetate	38	continuous	-	-
ZNO38c_400	nitrate	38	continuous	-	400
ZNO38c_450	nitrate	38	continuous	-	450
ZNO38c_500	nitrate	38	continuous	-	500
ZNOp3_400	nitrate	38	pulsed	3	400
ZNOp1_400	nitrate	38	pulsed	1	400

Table 2. Physicochemical properties of the ZnO samples: average crystallite size calculated from the (100) peak of wurtzite ZnO (d_{XRD}), specific surface area (S_{BET}), particle size (d_{DLS}), apparent band gap (E_g).

sample	d_{XRD} **(nm)**	$I_{(002)}/I_{(100)}$	S_{BET} **(g m^{-2})**	d_{DLS} **(nm)**	E_g **(eV)**
Zcom	43.0	0.87	10.8	230 ± 50	3.25
ZNOstir	21.6	1.26	0.4	1900 ± 200 5500 ± 300 (2%)	3.16
ZNOstir_400	22.4	0.90	5.1	1400 ± 200 5200 ± 400 (6%)	3.08
ZNO23c	19.0	1.13	12.0	420 ± 90	3.32
ZNO38c	19.0	1.09	11.9	430 ± 80	3.32
ZNO49c	20.1	1.07	12.5	410 ± 150	3.32
ZCl38c	19.9	1.00	32.6	90 ± 30	3.26
ZAc38c	26.7	0.96	18.5	220 ± 90 2800 ± 300 (4%)	3.28
ZNO38c_400	20.3	0.85	12.0	340 ± 170	3.20
ZNO38c_450	21.8	0.83	10.3	460 ± 190	3.17
ZNO38c_500	23.5	0.77	7.7	390 ± 120	3.18
ZNOp3_400	21.2	0.85	12.1	310 ± 120	3.20
ZNOp1_400	24.0	0.86	12.8	190 ± 120 750 ± 300 (6%)	3.16

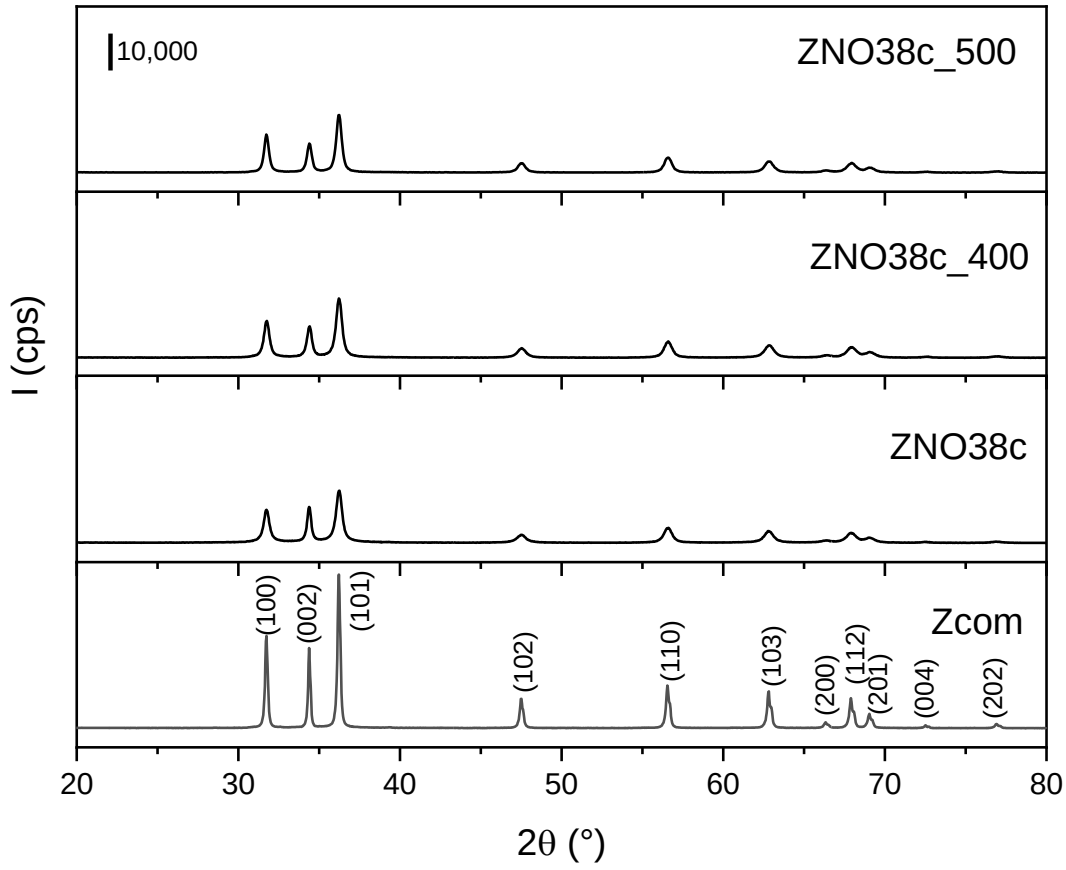
10,000
ZNO38c_500
ZNO38c_400
ZNO38c
Zcom
I (cps)
(100)
(002)
(101)
(102)
(110)
(103)
(200)
(112)
(201)
(004)
(202)
20
30
40
50
60
70
80
2θ (°)

Figure 1

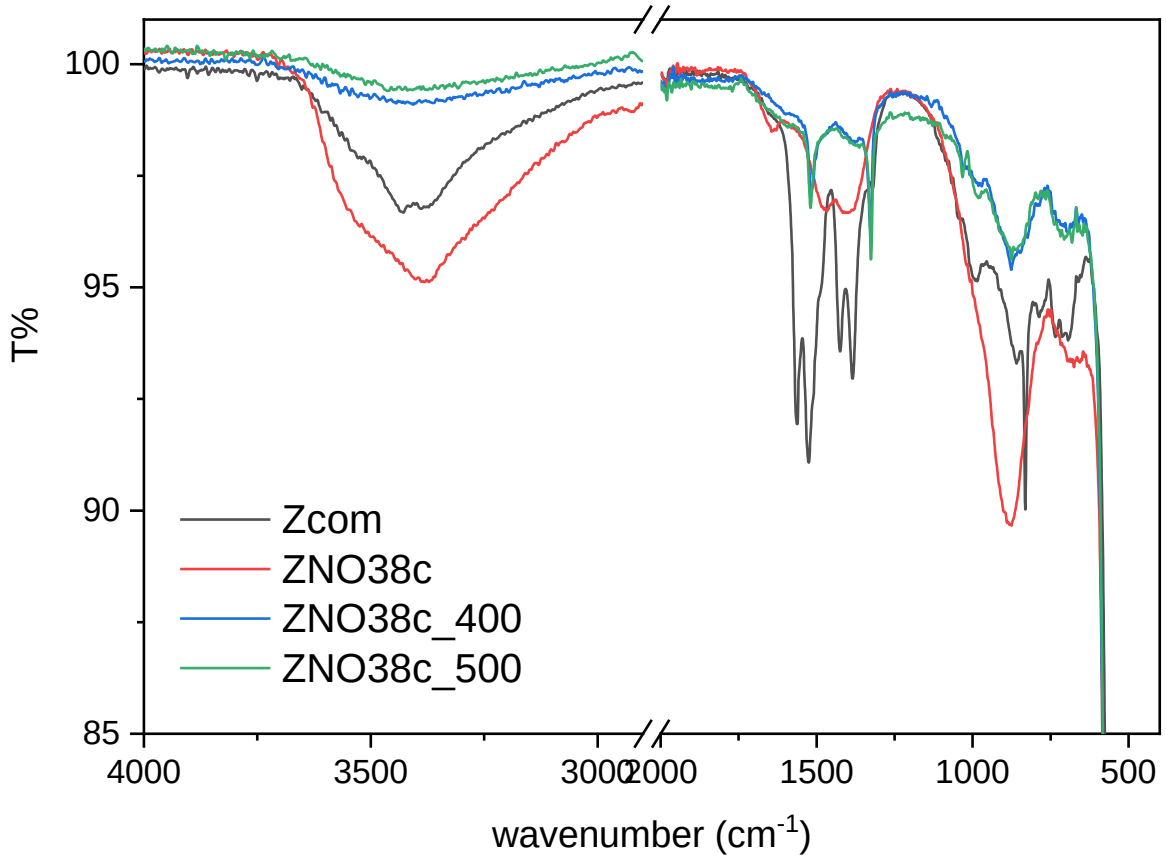
100
95
90
85
T%
4000
3500
3000
2000
1500
1000
500
wavenumber (cm-1)
Zcom
ZNO38c
ZNO38c_400
ZNO38c_500

Figure 2

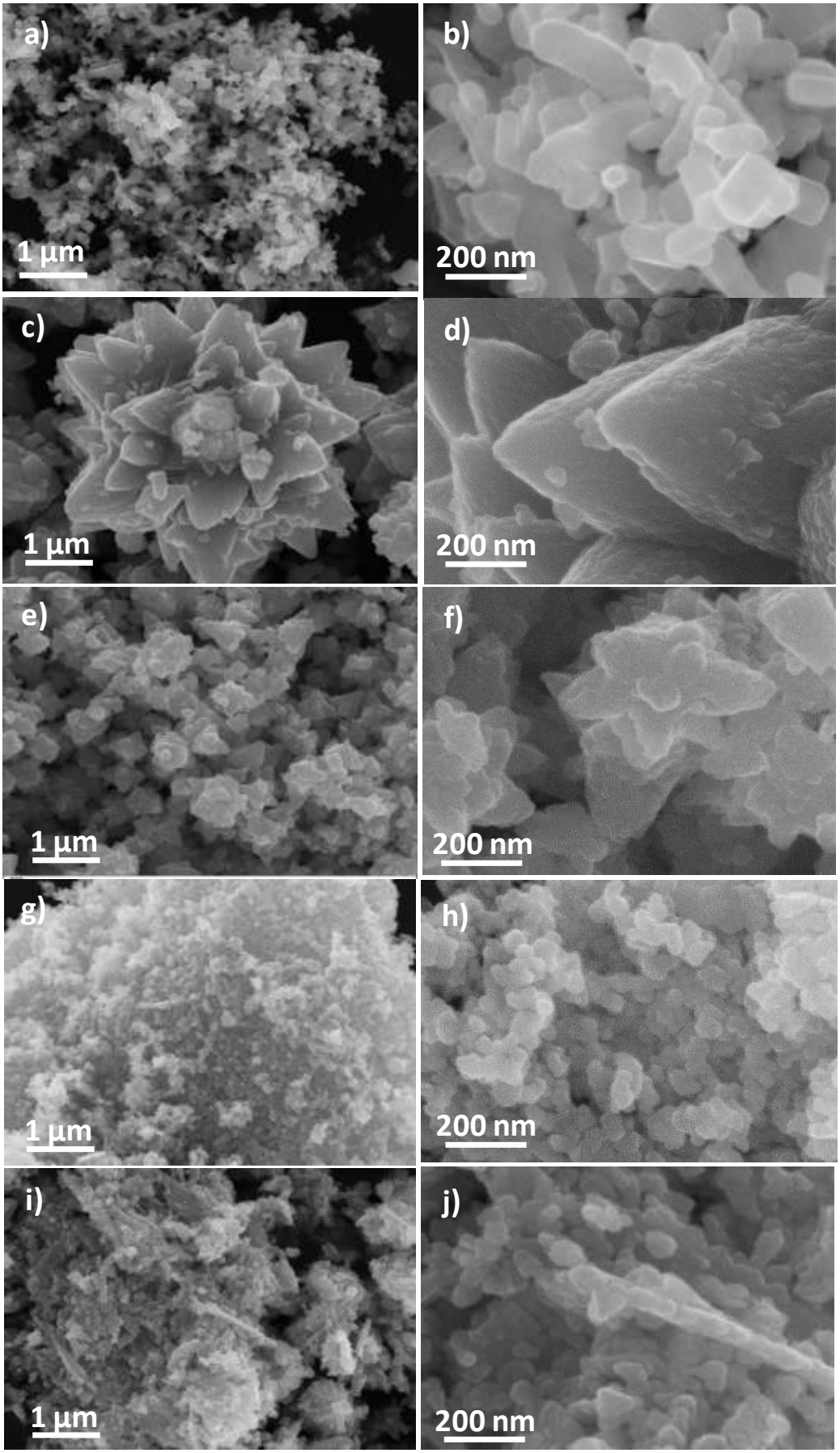
a)
1 µm
b)
200 nm
c)
1 µm
d)
200 nm
e)
1 µm
f)
200 nm
g)
1 µm
h)
200 nm
i)
1 µm
j)
200 nm

Figure 3

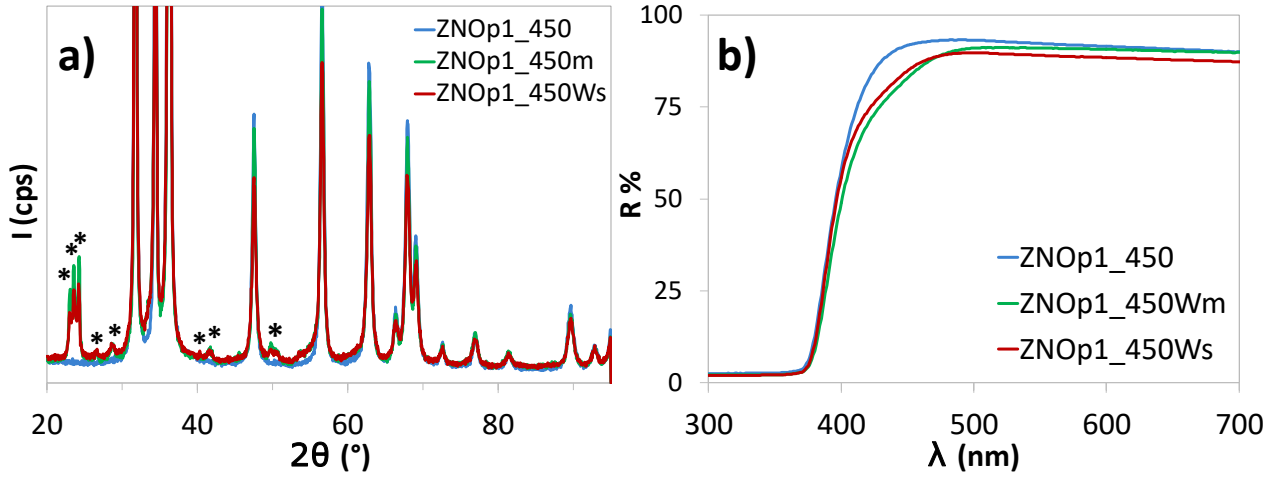
a)
ZNOp1_450
ZNOp1_450m
ZNOp1_450Ws
I (cps)
2θ (°)
b)
R %
λ (nm)
ZNOp1_450
ZNOp1_450Wm
ZNOp1_450Ws

Figure 4

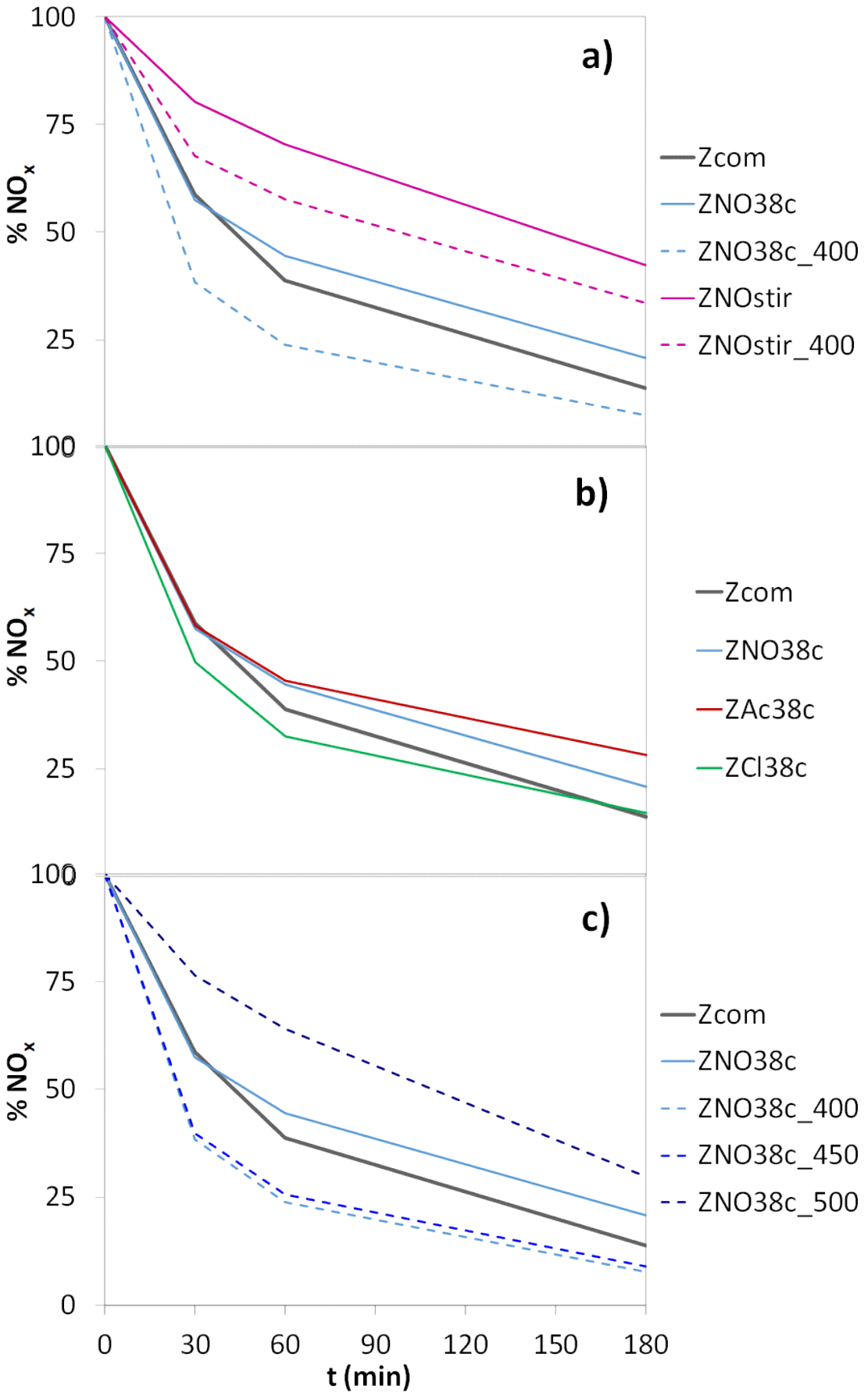
a)
b)
c)
% NOx
t (min)
0
25
50
75
100
0
30
60
90
120
150
180
Zcom
ZNO38c
ZNO38c_400
ZNOstir
ZNOstir_400
ZAc38c
ZCl38c
ZNO38c_450
ZNO38c_500

Figure 5

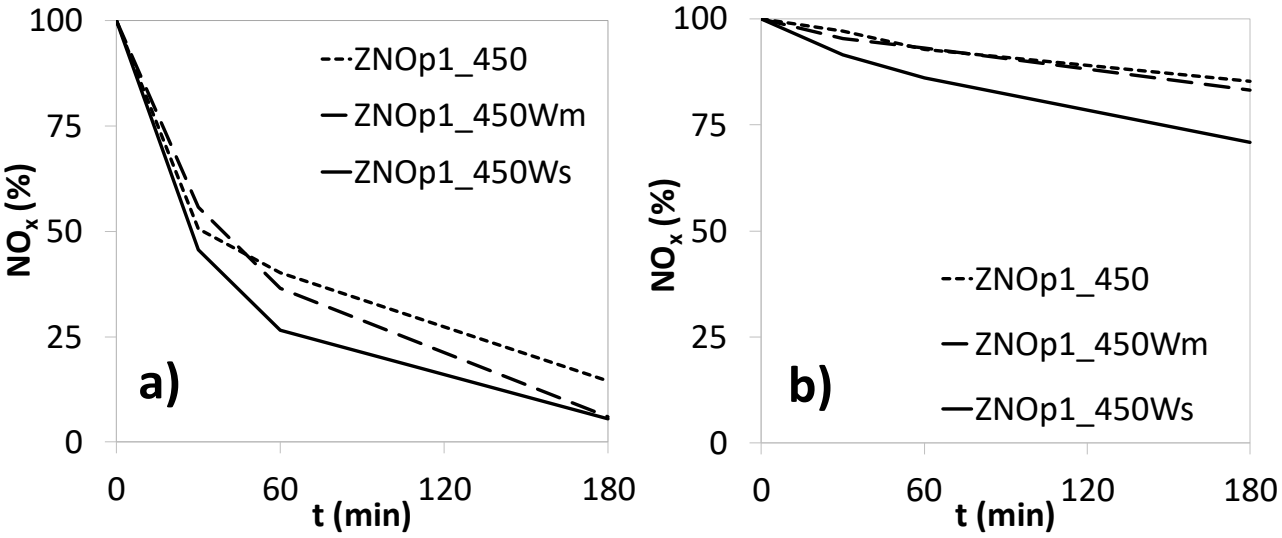
100
75
50
25
0
NOx (%)
---ZNOp1_450
— ZNOp1_450Wm
—ZNOp1_450Ws
a)
0
60
120
180
t (min)
b)

Figure 6

Figure captions

Figure 1 – Effect of calcination temperature on XRD patterns. The diffractogram of Zcom is reported as a reference.

Figure 2 – FTIR spectra of ZNO38c, ZNO38c_400, ZNO38c_500 and Zcom.

Figure 3 – SEM images of Zcom (a,b), ZNOstir (c,d), ZNO38c (e,f), ZClO38c (g,h), ZAc38c (i,j).

Figure 4 – XRD pattern (a) and DRS spectra (b) of ZNOp1_450, ZNOp1_450Wm and ZNOp1_450Ws. XRD peaks of monoclinic WO_3 are highlighted with a star.

Figure 5 – NO_x degradation curves under UV irradiation for ZnO samples: effect of sonication *vs.* stirring during synthesis (a), of adopted zinc source (b), of calcination temperature (c). The curve of Zcom is reported as a reference.

Figure 6 – NO_x degradation curves for ZnO-WO_3 composites under UV (a) and visible light (b) irradiation.